In Situ ATR-FTIR Study of the Cathode–Electrolyte Interphase: Electrolyte Solution Structure, Transition Metal Redox, and Surface Layer Evolution

Bertrand J. Tremolet de Villers,[a] Seong-Min Bak,[b] Junghoon Yang,[a] and Sang-Don Han*[a]

We present a study of the lithium nickel manganese cobalt oxide ($LiNi_{0.6}Mn_{0.2}Co_{0.2}O_2$, NMC622) cathode-electrolyte interphase (CEI) during galvanostatic charging and discharging using *in situ* attenuated total reflectance Fourier transform infrared (ATR-FTIR) methods to investigate the voltage dependent electrolyte solution structure changes at the interface, transition metal (TM) redox chemistry, and cathode/electrolyte interfacial layer evolution. Our *in situ* cell design provides both reliable electrochemical device testing and strong FTIR vibrational absorption signals near the cathode surface. Specifically, advanced spectral analysis elucidates changes of near-surface Li^+ ion (de)solvation by solvent molecules during galvanostatic cycling. Moreover, cathode metal-oxygen vibrational absorptions, sensitive to TM redox behaviors and subsequent local structural variations, were correlated to cathode de-lithiation (and lithiation) and electrolyte solution structure changes. In addition, we have detected the formation and evolution of a CEI surface layer on the NMC622 cathode that contributes to the cell's capacity fade.

1. Introduction

Rechargeable lithium-ion battery (LiB) technologies dominate the global marketplace for energy storage needs in portable electronic devices as well as within a rapidly-increasing demand for electric vehicle use.[1] In order to meet this growing demand and due to limited resources and fluctuating prices of current cathode elements, new battery materials with different chemical formulations must be developed to enable higher energy and power storage at lower cost. In the last decade, cathodes based on lithium nickel manganese cobalt oxide ($LiNi_{1-x-y}Mn_xCo_yO_2$ or NMC) have garnered much attention due to their high theoretical capacity up to 280 mAh g^{-1}.[2] In general, increasing the Ni content in these materials boosts the capacity, however this usually comes at the cost of decreased stability.[3] Thus, stabilization of the cathode-electrolyte interphase (CEI) is essential if high-voltage and low or no Co NMC-based cathodes are to be widely-adopted in application.[4]

To understand electrochemical cell degradation and failure mechanisms and develop mitigation strategies enabling long cycle life batteries with high energy density, significant effort has been devoted to spectroscopic investigations of batteries and their constituents.[5] Some example spectroscopies include X-ray based probes to obtain structural information about the materials and the local molecular bonding environment,[6] optical techniques such as UV-vis electronic absorption, infrared vibrational absorption, and Raman scattering to provide chemical information,[5b,7] as well as electron-based analytical tools including transmission electron microscopy (TEM) and scanning electron microscopy (SEM) for molecular level identification.[8] Most often, these techniques are applied *ex situ* to a component of the battery that has been harvested from a disassembled cell after testing. While informative, *ex situ* measurements cannot elucidate changes happening to the cell while testing, thus potentially failing to provide critical information about correlated processes governing cell performance.

Recently, we have developed *in situ* Raman and FTIR techniques applied to custom battery cells while simultaneously subjecting the cells to electrochemical testing.[9] The surface chemistry and evolution of the electrode-electrolyte interphase is monitored "in real-time" during cell charging and discharging cycles, providing a better understanding of the critical mechanisms underpinning the electrochemical performance of the batteries. For example, with our *in situ* methods, we can observe reversible evolution of a silicon anode-electrolyte interphase (SEI) component with a definitive peak assignment and show reversible silicon peak intensity changes upon lithiation and delithiation. These critical interfacial cell processes, that ultimately determine the battery's electrochemical performance, are not accessible with traditional *ex situ* measurements and underscore the importance of developing *in situ* spectroscopic techniques.

Here, we present how *in situ* attenuated total reflectance Fourier transform infrared (ATR-FTIR) methods can be used to

[a] *Dr. B. J. Tremolet de Villers, Dr. J. Yang, Dr. S.-D. Han*
Materials and Chemical Science and Technology Directorate
National Renewable Energy Laboratory
Golden, Colorado 80401, USA
E-mail: sang-don.han@nrel.gov
[b] *Dr. S.-M. Bak*
National Synchrotron Light Source II
Brookhaven National Laboratory
Upton, New York 11973, USA

Supporting information for this article is available on the WWW under https://doi.org/10.1002/batt.202000259

An invited contribution to a joint Special Collection between Batteries & Supercaps and Chemistry-Methods on In Situ and Operando Methods for Energy Storage and Conversion

study a model cathode – lithium nickel manganese cobalt oxide ($LiNi_{0.6}Mn_{0.2}Co_{0.2}O_2$, or NMC622) – during galvanostatic charging/discharging, and to monitor the cathode/electrolyte interphase interactions. In this study, we use Gen2 electrolyte (1.2 M lithium hexafluorophosphate ($LiPF_6$) in ethylene carbonate (EC):ethyl methyl carbonate (EMC), 3:7 wt%). Because vibrational absorptions are sensitive to the local bonding environment, our FTIR measurements distinguish between solvent molecules coordinating to a Li^+ ion (solvation) and free solvent molecules that do not interact with a Li^+ ion (desolvation) in the electrolyte within the CEI. Thus, we show how the solvent environment surrounding the Li^+ ion in the electrolyte near the cathode surface changes during charging (cathode de-lithiation) and discharging (cathode lithiation) of the battery, respectively. Furthermore, we observe that the cathode FTIR absorptions change due to local structural variations based on the redox behaviors of the transition metals (TMs) of the cathode during cycling. This TM redox-local structure variation dependence on measured cell voltage is corroborated by Ni K-edge X-ray absorption spectroscopy (XAS). In addition, we demonstrate how the surface sensitivity of the FTIR measurement enables monitoring of CEI formation and evolution during cell cycling beginning after the first few electrochemical cycles.

2. Results and Discussion

2.1. Construction of the Custom *In Situ* Cell

In order to perform *in situ* ATR-FTIR measurements of NMC622 while simultaneously subjecting it to galvanostatic electrochemical cycling, we have designed a custom cell holder (Figure 1a). The ATR-FTIR cell design concept was adapted from previous efforts by Ross *et al.* to study LiB anodes. Details of the measurement, including, for example, how the penetration depth of the evanescent IR wave changes with wavenumber can be found in some of their work.[10] In our design, a PEEK holder and lid assembly is affixed to an ATR-FTIR prism plate, creating an air-tight seal. The porous cathode as the working electrode is placed onto the surface of the prism, while lithium metal foil as counter/reference electrodes is attached to a stainless steel (SS316) spacer. When the lid is closed, a SS316 rod fit into the lid presses down on the "coin-type" cell to ensure good electrical contact between the electrodes, and the pressure also provides an intimate interface between the cathode surface and the ATR prism resulting in high FTIR signal intensity. By applying pressure to the cell with the stainless steel rod, we minimize buildup of internal cell resistance and observe no parasitic reactions from the cell components such as the current collectors or spacer. We demonstrate that our cell enables reliable and reproducible electrochemical performance, similar to a standard 2032 coin-type cell (Figure S1). A more detailed description of the porous cathode preparation, cell construction, and electrochemical testing is found in the Supporting Information.

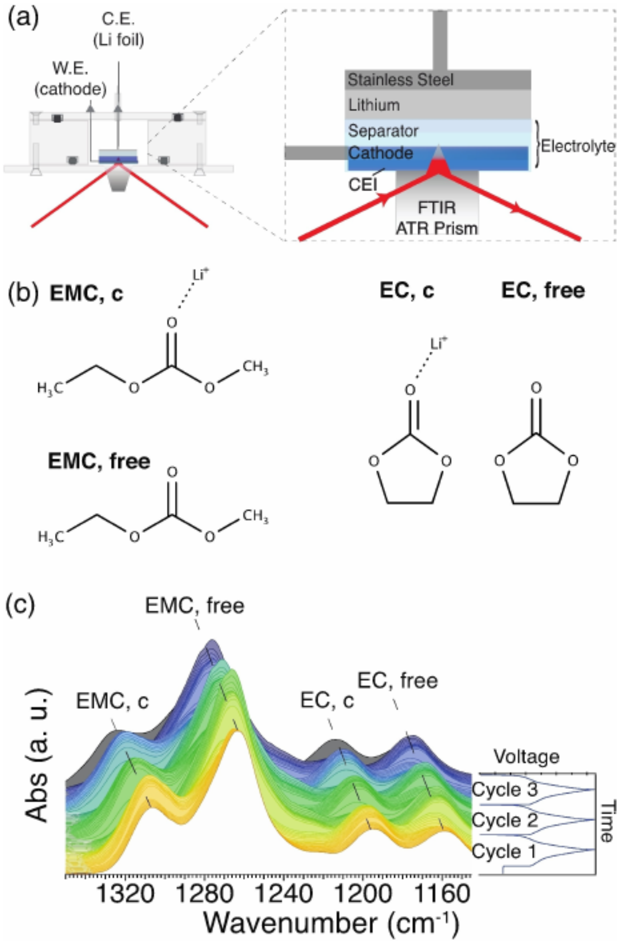

Figure 1. a) *In situ* ATR-FTIR cell design; b) molecular structures of ethyl methyl carbonate (EMC) and ethylene carbonate (EC), coordinated to a Li^+ ion and non-coordinated (free); c) *in situ* ATR-FTIR spectra of the EC and EMC solvent molecules (O=C–O bending modes) during the first two galvanostatic cycles at C/10 in the voltage range of 3.0–4.5 V (*vs* Li/Li^+).

2.2. Electrolyte Solution Structure

During galvanostatic cycling between 3.0–4.5 V (*vs* Li/Li^+, hereafter) at C/10 (1 C corresponding to a practical capacity of 200 $mAh\,g^{-1}$), we monitor the electrolyte solution structure changes near the cathode surface, as the IR evanescent wave probes 1–5 μm beyond the surface of the ATR prism.[10b] Importantly, infrared vibrational absorptions are sensitive to the solution components' local bonding environments. This enables the distinction between electrolyte species – EMC, EC, and PF_6^- – coordinated to nearby a Li^+ ion or "free", surrounded only by other solvent molecules.[11] The molecular structures of ethylmethyl carbonate (EMC) and ethylene carbonate (EC), coordinated to Li^+ ion and non-coordinated (free) are shown in Figure 1b. For example, a free EMC solvent molecule has an O=C–O bending mode vibrational absorption at 1263 cm^{-1}, but when solvating a Li^+ ion, the absorption shifts to 1306 cm^{-1}. Figure S2 shows the FTIR spectrum from 2000–400 cm^{-1} for Gen2 electrolyte and Table S1 lists the peak assignments for molecular bond vibrational absorptions of EC/EMC solvents and PF_6^- anion in the Gen2 electrolyte.[11b,12]

Figure 1c shows in situ ATR-FTIR vibrational absorption bands between 1330 and 1130 cm^{-1} focusing on O=C–O bending modes of the EC and EMC solvent molecules during the first three galvanostatic cycles. Band intensity changes are similar for other molecular vibrational modes of the solvents, for example the carbonyl (C=O) stretching between 1810 and 1700 cm^{-1}. To quantify changes in each of the FTIR absorption bands during cell cycling, linear regression peak fitting with a standard Voigt function model was used. As an example, the fit of the C=O stretching bands for a single spectrum and the changes in peak areas of the vibrational modes during cycling are presented in Figures S3a and S3b, respectively.

2.3. Transition Metal Redox

Use of a monolithic diamond ATR prism in our spectrometer permits acquisition of FTIR spectra down to 500 cm^{-1}, where metal-oxygen bond vibrational absorption occurs for the transition metals in NMC622. Despite a strongly absorbing P–F mode from the PF_6^- anion centered at 557 cm^{-1} and with a shoulder extending to 595 cm^{-1}, we have identified a broad cathode oxygen vibrational absorption from the NMC622 cathode between 570–610 cm^{-1}. Figure 2a shows *ex situ* ATR-FTIR spectra of NMC622 electrodes harvested at various state of charge (SOC) and depth of discharge (DOD) from one galvanostatic cycle in the voltage range of 3.0–4.5 V. The spectrum of pure Gen2 electrolyte is also included to show how it partially overlaps with the metal-oxygen band of the cathode. Upon partial delithiation (charging to 3.8 V) the metal-oxygen band shifts to higher energy. Further delithiation (charging above 4.0 V) results in a diminished signal, possibly due to increased electrical conductivity of the cathode that attenuates the IR excitation light.[13] Lithiation (discharging to 3.0 V) of the NMC622 results in a red shift of the metal-oxygen band, centered at 585 cm^{-1}, but not all the way back to the pristine state peak position at 571 cm^{-1}, possibly due to formation of a CEI layer and/or cathode structural changes from surface reconstruction at higher voltages, or simply because the cathode has not been relithiated to the same extent, especially since we did not apply a constant voltage at 3.0 V to fully lithiate the cathode and the part of the cathode

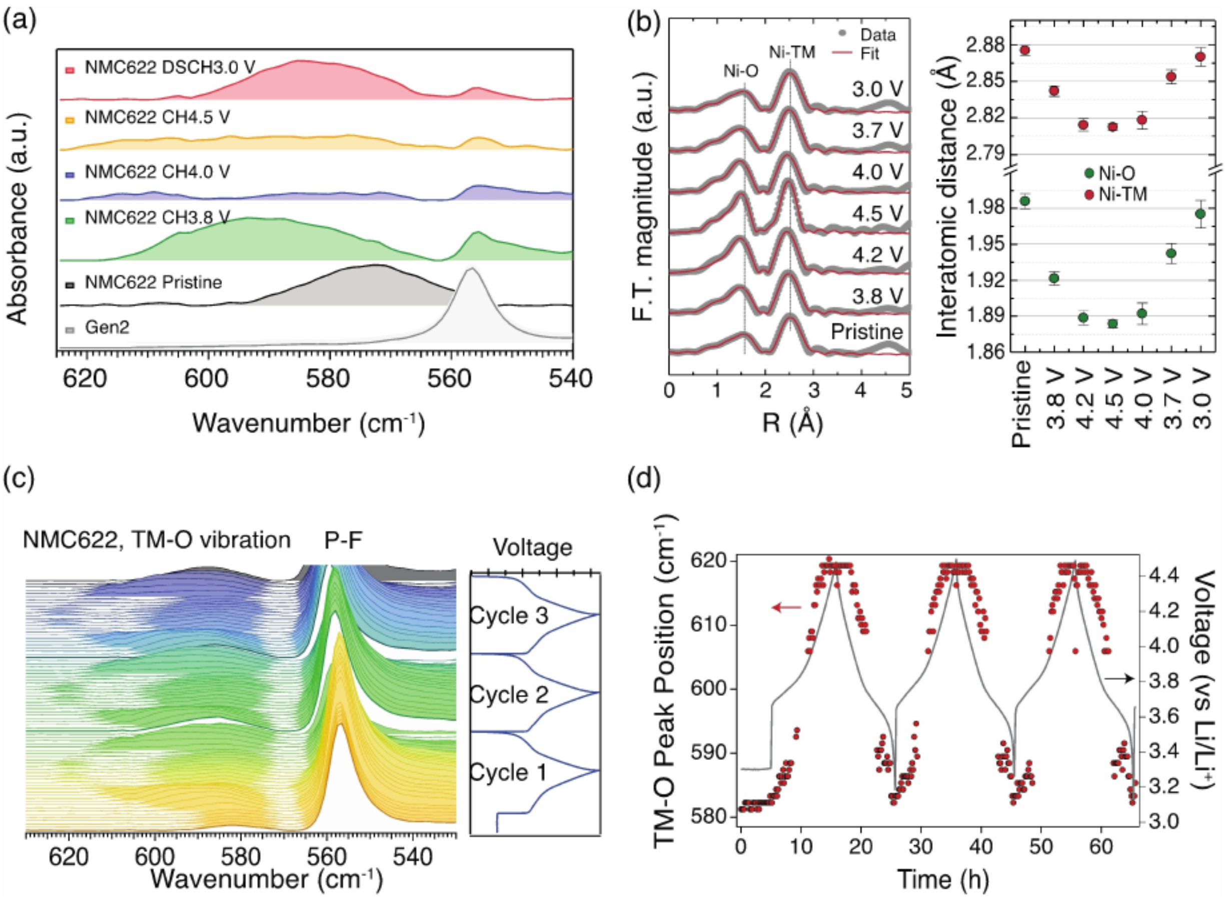

Figure 2. a) *Ex situ* ATR-FTIR spectra of the NMC622 electrodes at various SOC and DOD after one galvanostatic cycle at C/10 in the voltage range of 3.0–4.5 V (the spectrum of a Gen2 electrolyte is also included to show how it partially overlaps with the metal-oxygen band of the cathode, at around 585 cm^{-1}). b) Fourier transformed magnitude of Ni K-edge EXAFS spectra (dot) and fitting (line) and corresponding refined structural parameter of interatomic distance changes for the first shell (Ni–O) and second shell (Ni–TM (Ni/Mn/Co)). c) *In situ* ATR-FTIR spectra of the NMC622 electrodes, focusing on Ni–O interactions between 610–570 cm^{-1}, during the first three galvanostatic cycles at C/10 in the voltage range of 3.0–4.5 V. d) NMC622 transition metal (TM)-oxygen peak shift with cell voltage.

probed by the FTIR is furthest from the bulk electrolyte. We assign this broad peak between 570–610 cm^{-1} mainly to the oxygen atom lattice vibrations toward Li^+ vacancy sites in the crystal, based in part on the *in situ* Raman investigations by Flores *et al.* on similar cathode materials.[13b,14] This band involves Ni–O interactions, as the Ni^{2+}/Ni^{3+}/Ni^{4+} ions are the most electrochemically active cations in the cathode in the voltage range tested.[15]

To validate the Ni valence state changes probed by our ATR-FTIR technique, we performed *ex situ* TM K-edge X-ray absorption near edge structure (XANES) measurements, which are widely used for probing nominal valence state changes in an elementally selective way. Figures S4a and S4b show the normalized Ni K-edge XANES spectra during the first charge and discharge. The rigid edge shift to high energy during the charge process indicates the oxidation of Ni, while the shift to lower energy during the discharge process indicates the reduction of Ni. To quantify the Ni valence state, the half-height edge energies (i.e., $E_{0.5}$) are determined, along with NiO and $LiNiO_2$ references for comparison, as shown in Figure S4c. The pristine NMC622 electrode has nominal Ni valence of 2.67^+ based on its composition. Using the linear relationship between the valence state and $E_{0.5}$, the Ni valence at the fully charged state (4.5 V) becomes 4^+ (Figure S5). Overall, the edge shift of Ni K-edge XANES spectra is consistent with previous reports.[15b,16] This result confirms the full range of Ni redox-based charge compensation in NMC622 is achievable within our experimental conditions for the *in situ* ATR-FTIR technique. On the other hand, the corresponding K-edge XANES spectra of Mn and Co confirm that these ions are mostly electrochemically inactive in the applied voltage range (Figure S6a).

To verify the metal-oxygen vibrational absorption changes of the ATR-FTIR result, we conducted extended X-ray absorption fine structure (EXAFS) analysis. While the ATR-FTIR probes interface/near-surface structure, the EXAFS is a powerful technique to determine the changes in the local structure of the bulk materials. Figure 2b shows the Fourier transformed EXAFS spectra and their fitting result at the Ni K-edge for NMC622 at different charge and discharge states, as well as the corresponding refined structural parameter of interatomic distance (i.e., bond length) for the first shell (Ni–O) and the second shell (Ni–TM(Ni/Mn/Co)). Both interatomic distances of Ni–O and Ni–TM are contracted during the charging, from ~1.99 to 1.88 Å and ~2.88 to 2.81 Å, respectively, and expanded during the discharging process. This change of bond length is consistent with the Ni valence state changes. With the increase of Ni valence state (oxidation), the Ni–O and Ni–TM distance shorten during the charging and lengthen with Ni reduction during the discharging. No significant spectral changes are observed from Co and Mn K-edge EXAFS, which indicate the major structural changes during charge/discharge occurs at the Ni site (Figure S6b).

Figure 2c shows how the NMC622 metal-oxygen vibrational absorption band changes *in situ* during cell cycling for the first three galvanostatic charging/discharging cycles from 3.0 to 4.5 V. The *in situ* spectra agree well with the *ex situ* results but provide a much clearer picture of the voltage-dependent NMC622 absorption behavior. At the beginning of the charging, there is both an increase in absorption intensity and a shift of the peak to higher energy. The peak position is overlayed with the voltage profile in Figure 2d and suggests a continuous shift from 581 to 619 cm^{-1} during charging. While the peak continues to blue shift, the intensity reaches a maximum and then begins to decrease until it becomes negligible. Here, we are unable to calculate a meaningful peak position (Figure 2d) due to the lack of intensity. Interestingly, near the end of the charge, a small absorption feature around 619 cm^{-1} gains strength, and possibly indicates the presence of a different NMC622 phase near 4.5 V. Both the absorption band position and intensity behavior are fully reversable during discharging to 3.0 V. Although the EXAFS data pertains to the local structural changes in the NMC bulk, the extracted trend in Ni–O bond length is consistent with the FTIR data because as the Ni–O bond length decreases during charging, the NMC lattice vibrational modes will stiffen, resulting in an FTIR absorption at higher energies. The converse is true for the discharging behavior and a longer Ni–O bond length results in a red-shifted infrared absorption.

2.4. Relationship between Electrolyte Solution Structure and Cathode Transition Metal Redox

Based on the collected *in situ* ATR-FTIR spectra, we studied the relationship between the electrolyte solution structure and cathode transition metal redox chemistry (Figure 3). Figure 3b shows the O=C–O bending mode peak intensities of free EMC solvent molecules (EMC, free) and Li^+ ion coordinated EMC solvent molecules (EMC, coord.) bands at 1263 and 1306 cm^{-1}, respectively, as a function of the cell voltage (3.0–4.5 V) for the first three cycles. Previous FTIR studies have shown that when the electrode is polarized, changes in the electrolyte solution structure near the electrode surface are related to the formation of an electrode-electrolyte interphase.[17] According to the Stern model of electric double layers, during anodic polarization of the electrode, negative charge will compensate the electrode surface. Extending into the electrolyte just beyond that is the diffuse layer in which changes in electrolyte solvation behavior will be affected by the extent of electrode polarization. In the present case, it is expected that the equilibrium between free solvent molecules and solvent molecules coordinated to a Li^+ ion will shift towards the latter when the cathode potential is increased. Indeed, this is what we observe up to 3.8 V during charging. Above 3.8 V, however, we observe a drop in the intensity of EMC, coord. (and concomitant increase in the intensity of EMC, free), except for a small bump between 4.3 and 4.5 V (in the 2nd and 3rd cycles only). Furthermore, the intensities of the solvent peaks at a given voltage decrease after the first cycle, but then remain mostly constant during subsequent cycles, indicating that some solvent, especially EMC, may react to form the CEI during the first cycle. The sharp change in electrolyte solvation structure at 3.8 V corresponds to the end of the NMC622 hexagonal to monoclinic phase change after oxidation of Ni^{2+}

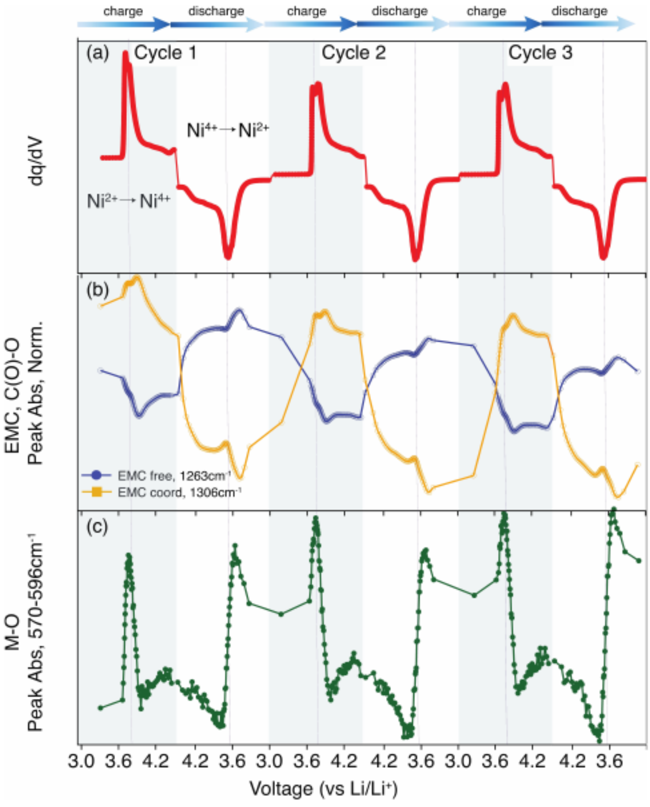

Figure 3. a) Differential capacity (d*q*/d*V*) of the *in situ* ATR-FTIR battery cell calculated for the first three galvanostatic cycles at C/10 in the voltage range of 3.0–4.5 V. b) Li^+ ion solvation and desolvation behaviors represented by the EMC $O{=}C{-}O$ bending mode absorption changes and c) the transition metal-oxygen (TM–O) vibrational absorption band intensity at between 580 and 620 cm^{-1} are correlated to the differential capacity (d*q*/d*V*). The shaded regions indicate the charging part of the cell cycling.

to $Ni^{3+/4+}$,[18] as shown in differential capacity plot in Figure 3a. Matsui *et al.* observed similar behavior in their FTIR study of surface layer formation of $LiMn_2O_4$ and $LiNi_{0.5}Mn_{1.5}O_4$ thin film electrodes.[19] During Ni^{2+} oxidation to $Ni^{3+/4+}$, the NMC622 lattice becomes strained since extraction of Li^+ ions from the lattice causes an increase in the electrostatic repulsion between adjacent metal-oxygen layers due to the negatively charged oxygen-oxygen interactions, as well as possible Ni^{3+} ion migration into Li^+ ion vacancy sites.[20] X-ray diffraction studies by Wang *et al.* have shown that the NMC622 layered crystal structure partially collapses above ~4.0 V, and there is some shrinkage of the cathode volume.[20] We postulate that the decrease in Li^+-coordinating solvent/increase in free solvent from 3.8 to 4.5 V is due to a relatively larger amount of "bulk" electrolyte that fills in the CEI around the reduced cathode volume. In other words, we are likely measuring electrolyte changes in the cathode pores where electrolyte that was previously in the bulk has now diffused into the extra space created in the pores.

In addition to investigating the electrolyte solution structure near the cathode surface, our ATR-FTIR technique is also able to probe the cathode material near surface. The peak intensity of the vibrational absorption band between 570–620 cm^{-1} as a function of cell voltage is presented in Figure 3c. The band intensity is related to the cathode TM redox behavior by comparing the peak intensity to the features in the differential capacity plot (Figure 3a). We observe that the metal-oxygen vibrational intensity and peak position (Figures 2c and 2d) are affected whenever local structural changes occur in the NMC622 due to the redox of the transition metals which we investigated with Ni K-edge EXAFS analysis (Figure 2b). The decrease in the NMC622 vibrational absorption between 3.8 and 4.5 V is likely due to the NMC622 exhibiting a greater electrical conductivity after the hexagonal to monoclinic phase transition, thus attenuating the penetration depth of the IR light. This phenomenon has been observed in similar cathode materials, particularly lithium manganese oxides and lithium cobalt oxides.[13a,21] The absorption intensity is recovered during discharge after $Ni^{3+,4+}$ reduction to Ni^{2+}, and subsequent phase transition back to hexagonal from monoclinic.

2.5. Cathode–Electrolyte Interphase (CEI)

It is known that NMC622 cathodes are usually coated with a thin (less than 10 nm) residue layer – mostly lithium carbonate (Li_2CO_3) originating from the synthesis reactants and storage environment – that plays an important role in the first-cycle gas evolution, electrolyte decomposition, and subsequent CEI formation.[22] Since the evanescent wave at the surface of the ATR prism extends 1–5 μm into the sample, in theory it should measure both the bulk and the surface of the cathode sample.[10b] To test this, we intentionally induced surface chemical changes by oxidizing an NMC811 composite electrode on a hot plate at 80 °C with 100% relative humidity for 395 hours, which should result in an even thicker Li_2CO_3 surface layer. NMC811 was chosen because it is more prone to surface oxidation than NMC622.[23] Indeed, after the damp heat treatment, the sample's FTIR spectrum (Figure S7a) exhibited additional peaks due to surface layer formation including carbonate species, confirming that our technique is surface sensitive. However, carbonate was not detected in the pristine sample before damp heat exposure, indicating that the surface sensitivity of the technique is not at the level of being able to detect an initial residue film. The results were also corroborated with Raman measurements of the samples (Figure S7b), and consistent with previous studies of NMC811 cathode air-sensitivity.[23] In addition, it is important to note that many of the surface species' absorptions in the FTIR measurements are obscured by the high-intensity absorptions of the electrolyte components in the *in situ* measurement.

Nevertheless, as shown in Figure 4, the *in situ* ATR-FTIR spectra collected during 8 cycles at C/10 in the voltage range of 3.0–4.5 V, do indicate growth of some CEI species and/or newly formed species in the bulk electrolyte starting in the 3rd cycle. Figure 4a shows 2-dimensional (2-D) spectral intensity maps of the *in situ* ATR-FTIR spectra between 1410–1480 cm^{-1}. As indicated by the color scale bars, lighter colors correspond to a relatively lower vibrational absorption intensity. The map on the left focusses on the region on the higher energy side of the EMC (free) methyl bending mode at 1450 cm^{-1}. Beginning

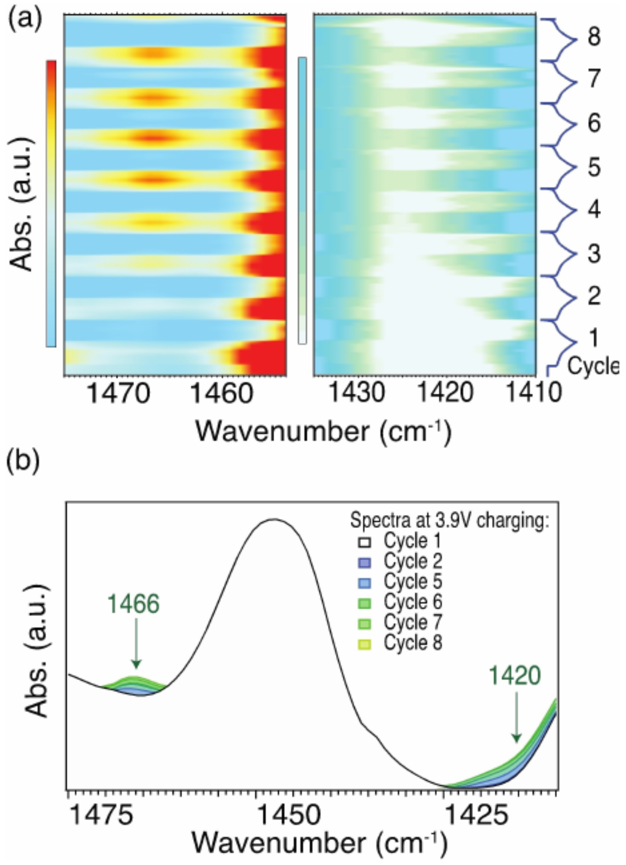

Figure 4. a) 2-D maps of the *in situ* FTIR spectral intensity between 1480 to 1415 cm^{-1}. b) *in situ* FTIR taken at 3.9 V during battery charging for the first 8 cycles.

in the 3rd cycle, there is clearly a new peak that appears at 1466 cm^{-1}, and it gains intensity in the cycles 4–6. Furthermore, the spectral intensity map on the right demonstrates broad absorption around 1420 cm^{-1} that also appears in the 3rd cycle and grows in subsequent cycles. We have yet to assign a definitive molecular origin for these features. Lithium carbonate, which has been studied as a surface layer on NMC cathodes, exhibits characteristic absorptions at 1490 and 1445 cm^{-1}, about 25–30 cm^{-1} shifted from where we observe features.[24] Interestingly, the 1466 cm^{-1} peak and band around 1420 cm^{-1} only appear during the charging, suggesting that the surface layer formation and/or newly formed species in the bulk electrolyte are dynamic with voltage and may be related to the TM redox chemistry. For example, surface nickel ions in a 4+ valence state are much more reactive that Ni^{2+} ions and cause more parasitic reactions are high voltage.[25] Furthermore, electrode-electrolyte interfacial surface layer components can be partially re-dissolved into the electrolyte depending on the electrode polarization. Such phenomena have been studied in detail for graphite anodes.[26] To further illustrate the emergence of the possible CEI formation and/or newly formed species in the bulk electrolyte in our system, Figure 4b displays the ATR-FTIR spectra, between 1480–1415 cm^{-1}, acquired at the same cell voltage (3.9 V) during charge for each of the first eight cycles. It is easy to see the growth of distinct peaks at 1420 and 1466 cm^{-1} that likely indicate growth of a carbonate surface species.

Finally, it should be noted that if the cathode is charged to a higher cut-off voltage, greater than 4.5 V, the transition metal cations in their high oxidation states can oxidize the electrolyte, resulting in CO_2 gas evolution that in turn yields some Li_2CO_3 solid and additional electrolyte decomposition products that become incorporated into the cathode surface.[27] Thus, with higher cut-off voltages, the *in situ* FTIR measurements should observe additional CEI species. These experiments are currently on-going and will be included in a future study. Overall, the experimental setup enables successful monitoring of the reversible electrochemical behaviors of the NMC622 electrode, Gen2 electrolyte, and newly formed CEI originating from electrolyte decomposition over repeated cycles.

3. Conclusions

In conclusion, we have shown how *in situ* ATR-FTIR can be used to investigate the cathode-electrolyte interfacial region during electrochemical cycling. Our study reveals three important aspects of the cell evolution: 1) solvation of the Li^+ ions by the solvent molecules near the cathode interface is related to the extent of electrode polarization and the (de)insertion of Li^+ ions from/into the NMC622 cathode during charging/discharging of the battery, 2) NMC622 lattice vibrational modes are correlated to local structural changes of the crystals, and possibly affected by the degree of Li^+ vacancies which eventually leads to a phase change, and 3) formation and evolution of the CEI can be monitored, which is important for evaluating the cell cycle lifetime and the nature of the cathode surface passivation. We have chosen NMC622 as a model cathode for our spectroscopic investigation, but we believe our approach will be useful to characterize novel cathode materials, next-generation anodes such as silicon, and new electrolyte solvent/additive formulations with potentially different solvation behavior. Furthermore, combining *in situ* analysis from infrared absorption with other complimentary techniques, for example Raman spectroscopy for bulk chemical identification and XPS for the local molecular bonding environment, will provide detailed chemical and mechanistic understanding of the critical processes occurring on the electrode surface and within the electrode-electrolyte interphase.

Experimental Section

Experimental details are included in the Supporting Information.

Acknowledgements

This work was authored in part by Alliance for Sustainable Energy, LLC, the manager and operator of the National Renewable Energy Laboratory (NREL) for the U.S. Department of Energy (DOE) under Contract No. DE-AC36-08GO28308. Support from the Vehicle

Technologies Office (VTO), Hybrid Electric Systems Program, David Howell (Manager), Battery R&D, Peter Faguy (Technology Manager), at the U.S. DOE, Office of Energy Efficiency and Renewable Energy, is gratefully acknowledged. The electrode active materials used in this article were synthesized at Argonne's Cell Analysis, Modeling and Prototyping (CAMP) Facility. Funding for in situ ATR-FTIR characterization provided in part by the Laboratory Directed Research and Development (LDRD) Program at NREL. The XAS research used beamline 7-BM (QAS) of the National Synchrotron Light Source II, a U.S. DOE Office of Science User Facility operated for the DOE Office of Science by Brookhaven National Laboratory (BNL) under Contract No. DE-SC0012704. The views expressed in the article do not necessarily represent the views of the DOE or the U.S. Government. The U.S. Government retains and the publisher, by accepting the article for publication, acknowledges that the U.S. Government retains a nonexclusive, paid-up, irrevocable, worldwide license to publish or reproduce the published form of this work, or allow others to do so, for U.S. Government purposes.

•

.

Keywords: *in situ* ATR-FTIR · cathode–electrolyte interphase · electrolyte solution structure · transition metal redox · surface layer evolution

[1] G. Zubi, R. Dufo-López, M. Carvalho, G. Pasaoglu, *Renewable Sustainable Energy Rev.* **2018**, *89*, 292–308.

[2] N. Nitta, F. Wu, J. T. Lee, G. Yushin, *Mater. Today* **2015**, *18*, 252–264.

[3] F. Schipper, E. M. Erickson, C. Erk, J.-Y. Shin, F. F. Chesneau, D. Aurbach, *J. Electrochem. Soc.* **2017**, *164*, A6220-A6228.

[4] J. R. Croy, A. Abouimrane, Z. Zhang, *MRS Bull.* **2014**, *39*, 407–415.

[5] a) A. M. Tripathi, W.-N. Su, B. J. Hwang, *Chem. Soc. Rev.* **2018**, *47*, 736–851; b) P. B. Balbuena, Y. X. Wang, *Lithium-ion Batteries: Solid-electrolyte Interphase*, World Scientific Publishing Company, **2004**.

[6] a) X. Liu, D. Wang, G. Liu, V. Srinivasan, Z. Liu, Z. Hussain, W. Yang, *Nat. Commun.* **2013**, *4*, 2568; b) P. Shearing, Y. Wu, S. J. Harris, N. Brandon, *Interface* **2011**, *20*, 43–47; c) S.-M. Bak, Z. Shadike, R. Lin, X. Yu, X.-Q. Yang, *NPG Asia Mater.* **2018**, *10*, 563–580.

[7] a) J. T. Li, Z. Y. Zhou, I. Broadwell, S. G. Sun, *Acc. Chem. Res.* **2012**, *45*, 485–494; b) E. Flores, P. Novák, E. J. Berg, *Front. Energy Res.* **2018**, *6*; c) V. Stancovski, S. Badilescu, *J. Appl. Electrochem.* **2013**, *44*, 23–43.

[8] a) Y. Yuan, K. Amine, J. Lu, R. Shahbazian-Yassar, *Nat. Commun.* **2017**, *8*, 15806; bJ. Wu, M. Fenech, R. F. Webster, R. D. Tilley, N. Sharma, *Sustain. Energy Fuels* **2019**, *3*, 1623–1646.

[9] a) B. J. Tremolet de Villers, Y. Ha, S.-D. Han, in *236th ECS Meeting (October 13–17, 2019)*, ECS, **2019**; b) Y. Ha, B. J. Tremolet de Villers, Z. Li, Y. Xu, P. Stradins, A. Zakutayev, A. Burrell, S. D. Han, *J. Phys. Chem. Lett.* **2020**, *11*, 286–291.

[10] a) F. Shi, P. N. Ross, H. Zhao, G. Liu, G. A. Somorjai, K. Komvopoulos, *JACS* **2015**, *137*, 3181–3184; b) F. Shi, P. N. Ross, G. A. Somorjai, K. Komvopoulos, *J. Phys. Chem. C* **2017**, *121*, 14476–14483.

[11] a) N. Chapman, O. Borodin, T. Yoon, C. C. Nguyen, B. L. Lucht, *J. Phys. Chem. C* **2017**, *121*, 2135–2148; b) A. V. Cresce, S. M. Russell, O. Borodin, J. A. Allen, M. A. Schroeder, M. Dai, J. Peng, M. P. Gobet, S. G. Greenbaum, R. E. Rogers, K. Xu, *Phys. Chem. Chem. Phys.* **2017**, *19*, 574–586.

[12] a) D. Aurbach, *J. Electrochem. Soc.* **1996**, *143*, 3809; b) D. M. Seo, S. Reininger, M. Kutcher, K. Redmond, W. B. Euler, B. L. Lucht, *J. Phys. Chem. C* **2015**, *119*, 14038–14046; c) S. Matsuta, T. Asada, K. Kitaura, *J. Electrochem. Soc.* **2000**, *147*, 1695; d) F. A. Miller, C. H. Wilkins, *Anal. Chem.* **1952**, *24*, 1253–1294; e) R. T. Pekarek, A. Affolter, L. Baranowski, J. Coyle, T. Hou, E. Sivonxay, B. A. Dougan, R. McAuliffe, K. Persson, B. Key, C. Apblett, G. M. Veith, N. R. Neale, *J. Mater. Chem. A* **2020**.

[13] a) C. Julien, M. Massot, *Phys. Chem. Chem. Phys.* **2002**, *4*, 4226–4235; b) E. Flores, N. Vonrüti, P. Novák, U. Aschauer, E. J. Berg, *Chem. Mater.* **2018**, *30*, 4694–4703.

[14] E. Flores, P. Novák, U. Aschauer, E. J. Berg, *Chem. Mater.* **2019**.

[15] a) H. Sun, K. Zhao, *J. Phys. Chem. C* **2017**, *121*, 6002–6010; b) C. Tian, D. Nordlund, H. L. Xin, Y. Xu, Y. Liu, D. Sokaras, F. Lin, M. M. Doeff, *J. Electrochem. Soc.* **2018**, *165*, A696-A704.

[16] a) C. Tian, Y. Xu, D. Nordlund, F. Lin, J. Liu, Z. Sun, Y. Liu, M. Doeff, *Joule* **2018**, *2*, 464–477; b) S.-M. Bak, E. Hu, Y. Zhou, X. Yu, S. D. Senanayake, S.-J. Cho, K.-B. Kim, K. Y. Chung, X.-Q. Yang, K.-W. Nam, *ACS Appl. Mater. Interfaces* **2014**, *6*, 22594–22601.

[17] a) S. Pérez-Villar, P. Lanz, H. Schneider, P. Novák, *Electrochim. Acta* **2013**, *106*, 506–515; b) J.-T. Li, S.-R. Chen, F.-S. Ke, G.-Z. Wei, L. Huang, S.-G. Sun, *J. Electroanal. Chem.* **2010**, *649*, 171–176; c) Y. Ikezawa, T. Ariga, *Electrochim. Acta* **2007**, *52*, 2710–2715; d) Y. Ikezawa, H. Nishi, *Electrochim. Acta* **2008**, *53*, 3663–3669.

[18] R. Jung, M. Metzger, F. Maglia, C. Stinner, H. A. Gasteiger, *J. Electrochem. Soc.* **2017**, *164*, A1361-A1377.

[19] M. Matsui, K. Dokko, K. Kanamura, *J. Electrochem. Soc.* **2010**, *157*, A121.

[20] Q. Wang, C.-H. Shen, S.-Y. Shen, Y.-F. Xu, C.-G. Shi, L. Huang, J.-T. Li, S.-G. Sun, *ACS Appl. Mater. Interfaces* **2017**, *9*, 24731–24742.

[21] M. Inaba, Y. Iriyama, Z. Ogumi, Y. Todzuka, A. Tasaka, *J. Raman Spectrosc.* **1997**, *28*, 613–617.

[22] a) S. E. Renfrew, B. D. McCloskey, *JACS* **2017**, *139*, 17853–17860; bS. E. Renfrew, B. D. McCloskey, *ACS Appl. Mater. Interfaces* **2019**, *2*, 3762–3772.

[23] R. Jung, R. Morasch, P. Karayaylali, K. Phillips, F. Maglia, C. Stinner, Y. Shao-Horn, H. A. Gasteiger, *J. Electrochem. Soc.* **2018**, *165*, A132-A141.

[24] I. H. Son, J. H. Park, S. Kwon, J. Mun, J. W. Choi, *Chem. Mater.* **2015**, *27*, 7370–7379.

[25] T. Li, X.-Z. Yuan, L. Zhang, D. Song, K. Shi, C. Bock, *Electrochem. Energy Rev.* **2020**, *3*, 43–80.

[26] S. J. An, J. Li, C. Daniel, D. Mohanty, S. Nagpure, D. L. Wood III, *Carbon* **2016**, *105*, 52–76.

[27] Y. Ruan, X. Song, Y. Fu, C. Song, V. Battaglia, *J. Power Sources* **2018**, *400*, 539–548.